Effects on the OTF of MSF structures with random variations

Kevin Liang, Miguel Alonso

Research Article | Vol. 27, No. 24 / 25 November 2019 / Optics Express 34665

Optics EXPRESS

Effects on the OTF of MSF structures with random variations

KEVIN LIANG[1,2] AND MIGUEL A. ALONSO[1,2,3,*]

[1]The Institute of Optics, University of Rochester, Rochester, NY 14627, USA
[2]Center for Freeform Optics, University of Rochester, Rochester, NY 14627, USA
[3]Aix Marseille Univ., CNRS, Centrale Marseille, Institut Fresnel, UMR 7249, 13397 Marseille Cedex 20, France
[*]miguel.alonso@fresnel.fr

Abstract: In diamond-machined freeform manufacturing processes, a tool-tip often leaves behind characteristic mid-spatial frequency (MSF) structures on the optical surface. Unwanted movement between the tool-tip and the part results in MSF structures with random variations. Here, we analyze the effects of these MSF structures on the system's optical performance and derive simple analytic estimates for the optical transfer function in terms of the parameters of these structures. These expressions are expected to aid in MSF tolerancing.

1. Introduction

Precision freeform manufacturing allows the fabrication of surfaces with large numbers of degrees of freedom. However, these processes typically involve the use of subaperture tools, which leave behind surface grooves whose characteristic frequencies are between those of figure and roughness. These errors, known as mid-spatial frequency (MSF) errors, introduce unwanted effects that are difficult to characterize and complicate tolerancing on manufactured parts [1,2].

In prior work, we explored the effects on the optical transfer function (OTF) of wavefront errors, including quadratic aberrations [3] as well as MSF groove structures due to subaperture tools [4]. In the latter case, two types of MSF groove errors common in freeform manufacturing processes were analyzed: parallel straight grooves resulting from diamond milling, and concentric circular (or spiral) grooves resulting from diamond turning. The key theoretical tool proposed there to obtain analytic expressions for the OTF was referred to as the pupil-difference probability density (PDPD), which is defined as the probability density that two random points in the pupil with given vector separation have a given difference in wavefront error. This prior study assumed regular grooves of equal height and width [4]. However, real processes present tool-tip or spindle vibrations, causing the MSF structures to have profiles are not perfectly periodic. Diamond machining usually involves a fixed tool-tip that makes contact with the optical part as the part is moving (rotating or translating). A local coordinate system is used in which the three directions are called the thrust, *cutting*, and *feed* directions of the machine, as shown in Fig. 1(a). It is well established that there can be tool-tip vibration in all three of these directions [5–10], and so incorporating such effects into the models for the OTF is of central importance. Vibrations in the thrust and cutting directions cause random variations t_i in the depth of each groove, following a probability density $K_{\mathrm{T}}(t_i)$ with standard deviation μ, as shown in Fig. 1(c). Vibrations in the feed direction, on the other hand, introduce random lateral groove displacements f_i following a probability density $K_{\mathrm{F}}(f_i)$ with standard deviation σ. Our goal is to provide simple approximate formulas for the OTF of milled and turned surfaces that incorporate these effects.

The outline of this work is as follows: A review of the PDPD is provided in Sec. 2. The analysis of MSF structures including the effects of tool-tip vibrations is given in Sec. 3 for milled surfaces and in Sec. 4 for turned surfaces. For readers more interested in the formulas than the formal derivations, Sec. 5 provides a self-contained summary of the main results.

#377395 https://doi.org/10.1364/OE.27.034665
Journal © 2019 Received 10 Sep 2019; revised 31 Oct 2019; accepted 31 Oct 2019; published 11 Nov 2019

Optics EXPRESS

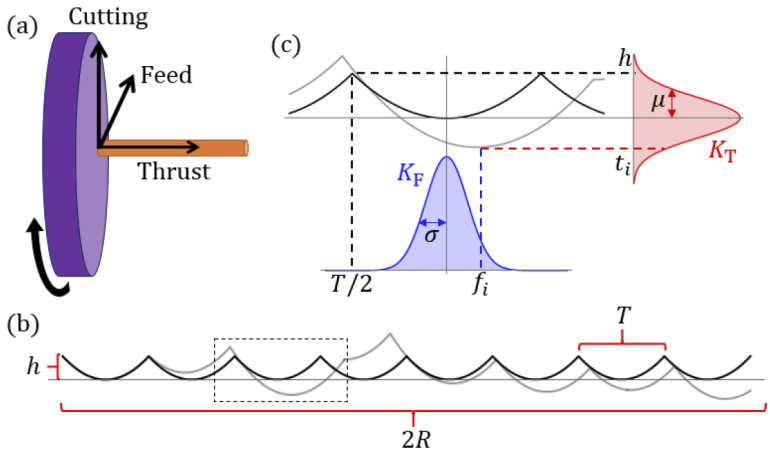

Fig. 1. (a) Diagram of the tool-tip (orange) and the rotating optical part (purple) in a diamond-turning process, and the three directions of possible vibrations. (b) Nominal MSF structure (black) with height h and period T. The size of the pupil is $2R$, twice the radius. An example of a MSF structure with random variations is also shown (gray). A sample cycle from (b) is shown in (c) with the probability densities K_T (red, with uncertainty μ) governing thrust (and cutting) vibrations, and K_F (blue, with uncertainty σ) governing feed vibrations.

2. Review of general PDPD theory

The PDPD, denoted as $P(\eta,\ \boldsymbol{\rho})$, is defined as the probability density that for two random points in the system's pupil whose vector separation is $\boldsymbol{\rho}$, the difference in aberration function W is equal to some prescribed quantity η. Mathematically, this can be written in the following form:

$$P(\eta,\ \boldsymbol{\rho}) \triangleq \frac{\int_{O(\boldsymbol{\rho})} \delta\{\eta - [W(\boldsymbol{q}-\boldsymbol{\rho}/2) - W(\boldsymbol{q}+\boldsymbol{\rho}/2)]\}\,\mathrm{d}^2q}{\int_{O(\boldsymbol{\rho})} \mathrm{d}^2q}, \tag{1}$$

where $\triangleq$ denotes a definition, δ is the Dirac delta distribution, and $O(\boldsymbol{\rho})$ is the overlap region of two pupil copies separated by $\boldsymbol{\rho}$. Note that the area of $O(\boldsymbol{\rho})$ normalized by its value at $\boldsymbol{\rho} = \mathbf{0}$ gives precisely the OTF for a perfect unaberrated system. In the case of a system with a circular pupil of radius R (say, in units of NA or spatial frequency), the perfect system's OTF depends only on $\rho = |\boldsymbol{\rho}|$ and is given by [11]

$$\mathrm{OTF}_{\mathrm{perf}}(\rho) = \frac{\int_{O(\boldsymbol{\rho})} \mathrm{d}^2q}{\int_{O(\mathbf{0})} \mathrm{d}^2q} = \frac{2}{\pi}\left[\cos^{-1}\left(\frac{\rho}{2R}\right) - \frac{\rho}{2R}\sqrt{1-\left(\frac{\rho}{2R}\right)^2}\right]. \tag{2}$$

The usefulness of the PDPD stems from its one-dimensional Fourier relation with the OTF:

$$\mathrm{OTF}(k,\ \boldsymbol{\rho}) = \mathrm{OTF}_{\mathrm{perf}}(\boldsymbol{\rho})\tilde{P}(k,\ \boldsymbol{\rho}) = \mathrm{OTF}_{\mathrm{perf}}(\boldsymbol{\rho})\int P(\eta,\ \boldsymbol{\rho})\exp(\mathrm{i}k\eta)\,\mathrm{d}\eta, \tag{3}$$

where the tilde denotes a Fourier transform from error difference η to wavenumber k. As was shown in [3] and [4], working with the PDPD rather than directly with the OTF allows geometrical insights that lead to useful approximations. This is also the case in the treatment that follows.

3. Effects of tool-tip vibrations in MSF structures for milled surfaces

The PDPD due to parallel MSF grooves (e.g. resulting from diamond milling) can be approximately expressed in terms of the one-dimensional PDPD of its cross-section [4] by using the scalar pupil

Optics EXPRESS

displacement variables $q_n = \boldsymbol{q} \cdot \hat{n}$ and $\rho_n = \boldsymbol{\rho} \cdot \hat{n}$, where $\hat{n}$ is the unit vector normal to the grooves. The grooves of the nominal MSF structure (without tool-tip vibrations) can be modeled as a piecewise-parabolic function, where h and T are the grooves' nominal peak-to-valley (PV) and width (or period), respectively, as illustrated in Fig. 1(b). It was shown in [4] that such a MSF structure leads to a very simple nominal PDPD (and Fourier transform):

$$P_1(\eta, \rho_n) = \frac{1}{w_0(h, T, \rho_n)} \text{rect}\left[\frac{\eta}{w_0(h, T, \rho_n)}\right] \quad \text{and} \quad \tilde{P}_1(k, \rho_n) = \text{sinc}\left[k w_0(h, T, \rho_n)/2\right], \quad (4)$$

where $w_0(h, T, \rho_n) = 8h\hat{\rho}_+\hat{\rho}_-$, with $\hat{\rho}_+ = (\rho_n/T) \bmod 1$, $\hat{\rho}_- = (1 - \rho_n/T) \bmod 1 = 1 - \hat{\rho}_+$, and $\text{rect}(u) = 1$ for $|u| \le 1/2$ and zero otherwise. The fact that P_1 in Eq. (4) takes the form of a rectangle function can be understood from Fig. 2 where we see that the difference of two displaced versions of W takes on a regular piecewise-linear sawtooth shape (gray lines) constrained in η to a localized region of width w_0.

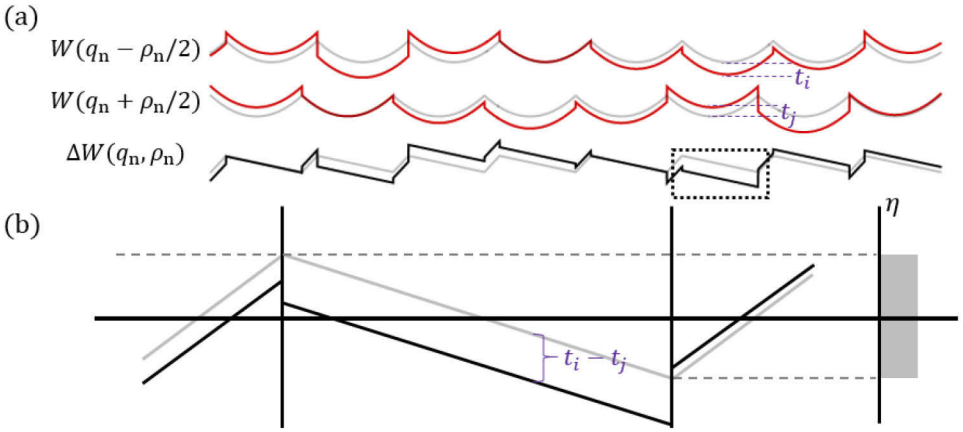

Fig. 2. (a) Two oppositely shifted copies of W, along with their difference ΔW, where t_i and t_j denote the vertical shift of each parabolic segment for $W(q_n - \rho_n/2)$ and $W(q_n + \rho_n/2)$, respectively, due to thrust vibration. (b) Zoom for one quasi-period, where the effect of thrust vibration is seen to correspond to a vertical shift defined by the difference $t_i - t_j$.

At this point, it is useful to define the transition function $\mathcal{T}_{\rho_n}$ as

$$\mathcal{T}_{\rho_n}(f,\ g) \triangleq \text{Max}\left(1 - \frac{\rho_n}{T}, 0\right) f + \text{Min}\left(\frac{\rho_n}{T}, 1\right) g, \quad (5)$$

for any f and g. Clearly, $\mathcal{T}_{\rho_n}$ gives rise to a linear transition between f and g as ρ_n passes through the first period. This is useful in Secs. 3 and 4 because the PDPD involves the difference of two copies of W displaced by ρ_n. When $\rho_n < T$, this difference includes points from the same period. Although this is unimportant when the MSF structure is periodic (nominal), it is necessary to use $\mathcal{T}_{\rho_n}$ to account for the case when random variations are introduced to each period independently.

3.1. Pistons model for thrust vibrations

Let us start by considering fluctuations in the height of the ridges resulting from variations in thrust (or cutting). We model these fluctuations by letting each parabolic segment be shifted vertically by an amount t_i, where each shift is assumed to be independent from all others, following a zero-mean probability density $K_T(t_i)$ whose standard deviation μ is assumed to be small compared to h [see Fig. 1(c)]. To begin, we try an overly simplistic model that we call the *pistons model*, where each complete parabolic segment is rigidly displaced, causing unphysical

Optics EXPRESS

discontinuities in W as illustrated in Fig. 2(a). The difference of the two oppositely-shifted copies of the error, $\Delta W = W(q_n - \rho_n/2) - W(q_n + \rho_n/2)$, is then also discontinuous.

One can see from Fig. 2 that the rectangular contribution for each straight segment of ΔW is shifted in η by the difference $t_i - t_j$. Hence, the mean effect of thrust vibrations is simply given by

$$P_{1,T}(\eta, \rho_n) = \iint_{-\infty}^{\infty} K_T(t_i) K_T(t_j) P_1[\eta - (t_i - t_j)]\, dt_i\, dt_j. \tag{6}$$

Equation (6) has the form of a double convolution, so in the Fourier domain it becomes a product:

$$\tilde{P}_{1,T}(k, \rho_n) = \tilde{K}_T^2(k) \tilde{P}_1(k, \rho_n). \tag{7}$$

Estimated forms for the probability densities K_T are reported in the literature [5,9,10], with models that are based on studies of tool-tip and spindle resonance frequencies. The resulting distribution (and its Fourier transform) governing thrust vibrations is given by

$$K_T(t) = \mathrm{Re}\left(\frac{1}{\pi\sqrt{2\mu^2 - t^2}}\right) \quad \text{and} \quad \tilde{K}_T(k) = J_0\left(\sqrt{2}k\mu\right), \tag{8}$$

where J_0 is the zeroth order Bessel function of the first kind. This leads to the simple expression

$$\tilde{P}_{1,T}(k, \rho_n) = J_0^2\left(\sqrt{2}k\mu\right) \tilde{P}_1(k, \rho_n). \tag{9}$$

Note that the difference between the two shifted copies of W in Fig. 2(a) were assumed to involve different parabolic segments, with independent shifts t_i and t_j. This is a valid assumption as long as $\rho_n \geq T$. When $\rho_n < T$, the PDPD includes a contribution from the differences of each groove with a displaced version of itself, and hence proportional to P_1, the nominal PDPD. The weight of this contribution diminishes proportionally to $T - \rho_n$ as ρ_n increases, and disappears completely once $\rho_n \geq T$. Hence, we construct the OTF estimate by using the linear transition function in Eq. (5) in the form $\mathrm{OTF}(k, \rho_n) \approx \mathrm{OTF}_{\mathrm{perf}}(\rho) \mathcal{T}_{\rho_n}(\tilde{P}_1, \tilde{P}_{1,T})$. Figure 3 shows comparisons of this OTF estimate with the average of several numerically computed OTFs of simulated realistic realizations of such surfaces with the corresponding statistics, for several values of the ratio μ/h. In these simulations, each parabolic segment is assigned a random shift t_i but the resulting surface is made continuous by extending the lower parabolic segment in each intersection. The plots show that the pistons model predicts well the local maxima of the OTF, but fails even for moderate values of μ/h near the minima ($\hat{\rho}_+ \approx 1/2$), where the effects of the unphysical discontinuities in W are exacerbated.

3.2. Realistic model for thrust vibrations

It turns out that an expression can be found based on a more realistic model with continuous grooves, whose form is almost as simple as that of the pistons model. The key is to study the shift s of the intersections of each segment of ΔW. As can be seen from Fig. 4(b), s depends not only on ρ_n but also on the shifts t_i and t_{i+1} of two contiguous grooves, as well as on the shift t_j of the groove in the displaced replica that overlaps with this junction. The value of s can be found from simple geometric considerations to be

$$s(t_i,\ t_{i+1},\ t_j, \rho) = (t_i - t_j)\hat{\rho}_+ + (t_{i+1} - t_j)\hat{\rho}_-, \tag{10}$$

Because the slopes of the segments of ΔW do not change with these shifts, no scaling factor of the probability density accompanies them. Since all intersections, whether they correspond to positive or negative ΔW, undergo shifts of this type, the average effect of thrust vibrations is

Optics EXPRESS

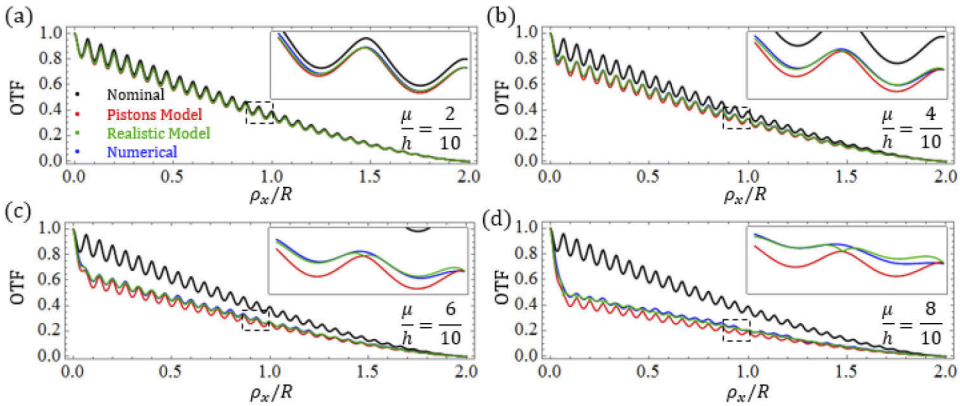

Fig. 3. OTF sections for various values of μ/h, for $kh = 1$ and 30 cycles across the aperture. In each part, the nominal (black) OTF corresponds to the case of $\mu = 0$, the numerical (blue) OTF is the average OTF from 30 randomly generated [with K_{T} given by Eq. (8)] MSF surfaces, and the theoretical models are calculated from Eq. (9) (red) and Eq. (14) (green).

encapsulated by averaging versions of the nominal distributions shifted by s, weighted by the probability densities of the displacements of the grooves:

$$P_{1,\mathrm{T}}(\eta,\rho_{\mathrm{n}}) = \iiint_{-\infty}^{\infty} K_{\mathrm{T}}(t_i)K_{\mathrm{T}}(t_j)K_{\mathrm{T}}(t_{i+1})P_1\left[\eta - s(t_i,\ t_{i+1},\ t_j,\rho_{\mathrm{n}}),\rho_{\mathrm{n}}\right]\,\mathrm{d}t_i\mathrm{d}t_{i+1}\mathrm{d}t_j. \tag{11}$$

It is convenient to perform a change of variables so that $s = (t_i - t_j)\hat{\rho}_+ + (t_{i+1} - t_j)$ is one of the variables of integration along with $a = t_1$ and $b = t_{i+1}$. With this, Eq. (11) can be rewritten as

$$P_{1,\mathrm{T}}(\eta,\rho_{\mathrm{n}}) = \int_{-\infty}^{\infty}\left[\iint_{-\infty}^{\infty} K_{\mathrm{T}}(a)K_{\mathrm{T}}(b)K_{\mathrm{T}}(a\hat{\rho}_+ + b\hat{\rho}_- - s)\,\mathrm{d}a\,\mathrm{d}b\right]P_1(\eta - s,\rho_{\mathrm{n}})\,\mathrm{d}s. \tag{12}$$

Equation (12) can be viewed as a triple convolution, so in the Fourier domain we have

$$\tilde{P}_{1,\mathrm{T}}(k,\rho_{\mathrm{n}}) = \tilde{K}_{\mathrm{T}}(k)\tilde{K}_{\mathrm{T}}(k\hat{\rho}_+)\tilde{K}_{\mathrm{T}}(k\hat{\rho}_-)\,\tilde{P}_1(k,\rho_{\mathrm{n}}). \tag{13}$$

Note that Eq. (13) differs from the result for the pistons model, Eq. (7), in that it has three factors of the characteristic function $\tilde{K}_{\mathrm{T}}$; furthermore, the arguments of two of these are dependent on ρ_{n}.

For K_{T} given by Eq. (8), we have the following simple expression for $\tilde{P}_{1,\mathrm{T}}(k,\rho_{\mathrm{n}})$:

$$\tilde{P}_{1,\mathrm{T}}(k,\rho_{\mathrm{n}}) = J_0\left(\sqrt{2}k\mu\right)J_0\left(\sqrt{2}k\mu\hat{\rho}_+\right)J_0\left(\sqrt{2}k\mu\hat{\rho}_-\right)\tilde{P}_1(k,\rho_{\mathrm{n}}). \tag{14}$$

Figure 3 shows comparisons of $\mathrm{OTF}_{\mathrm{perf}}(\rho)\mathcal{T}_{\rho_{\mathrm{n}}}(\tilde{P}_1,\tilde{P}_{1,\mathrm{T}})$ where $\tilde{P}_{1,\mathrm{T}}$ is given by Eq. (14), with numerically-computed OTFs for several values of the ratio μ/h. Compared with the pistons model's result in Eq. (7), it is evident that Eq. (14) is more accurate, particularly near the local minima of the OTF.

Although the form of K_{T} in Eq. (8) is a realistic model for thrust vibrations, it is worth noting that a zero-mean Gaussian form for K_{T} of the same standard deviation, namely

$$K_{\mathrm{T}}(t) = \frac{1}{\sqrt{2\pi}\mu}\exp\left(-\frac{t^2}{2\mu^2}\right) \quad \text{and} \quad \tilde{K}_{\mathrm{T}}(k) = \exp\left(-\frac{k^2\mu^2}{2}\right), \tag{15}$$

predicts very similar results for the OTF. This is because it is the characteristic functions (and not the probability densities) that appear as factors in Eq. (13), and the characteristic functions in Eqs. (8) and (15) largely agree for $k\mu < 1$. Under this assumption, $\tilde{P}_{1,\mathrm{T}}$ can be written as

$$\tilde{P}_{1,\mathrm{T}}(k,\rho_{\mathrm{n}}) = \exp\left[-\frac{k^2\mu^2}{2}\left(\hat{\rho}_+^2 + \hat{\rho}_-^2 + 1\right)\right]\tilde{P}_1(k,\rho_{\mathrm{n}}). \tag{16}$$

Optics EXPRESS

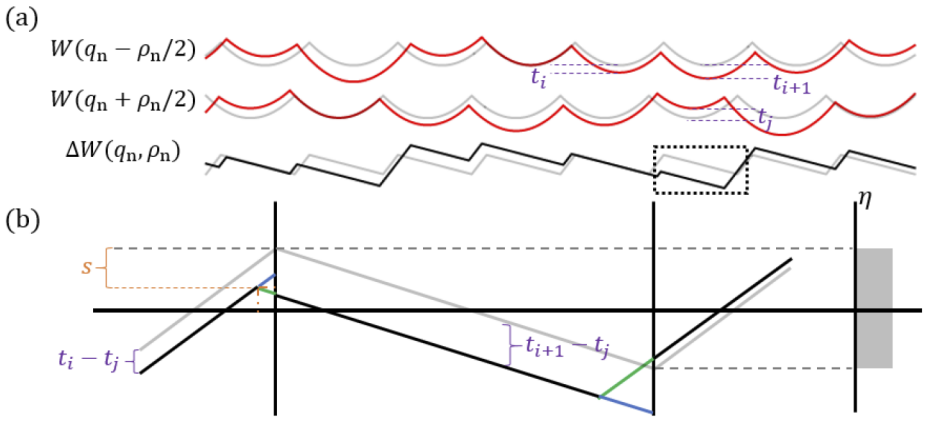

Fig. 4. (a) Two oppositely shifted copies of W, along with their difference ΔW, where t_i and t_j denote the vertical shift of each parabolic segment for $W(q_n - \rho_n/2)$ and $W(q_n + \rho_n/2)$, respectively, due to thrust vibration. (b) Zoom for one quasi-period, where the effect of thrust vibration is seen to correspond to a vertical shift s of the intersection points, which is defined in terms of ρ, t_i, t_{i+1}, and t_j.

3.3. *Feed vibrations model*

We now model the effects of feed vibrations by letting each parabolic segment of the groove structure be displaced laterally by an amount f_i, as shown in Fig. 5(a). The displacements f_i follow a zero-mean probability density K_F whose standard deviation σ is assumed to be small compared to the nominal groove width T [see Fig. 1(c)]. These displacements modify the saw-tooth structure of ΔW such that (unlike for thrust vibrations) the slopes of the different line segments in ΔW change, as shown in Fig. 5(b). Therefore, not only do the limits of the contributions to the PDPD change with the fluctuations, but also their relative weights.

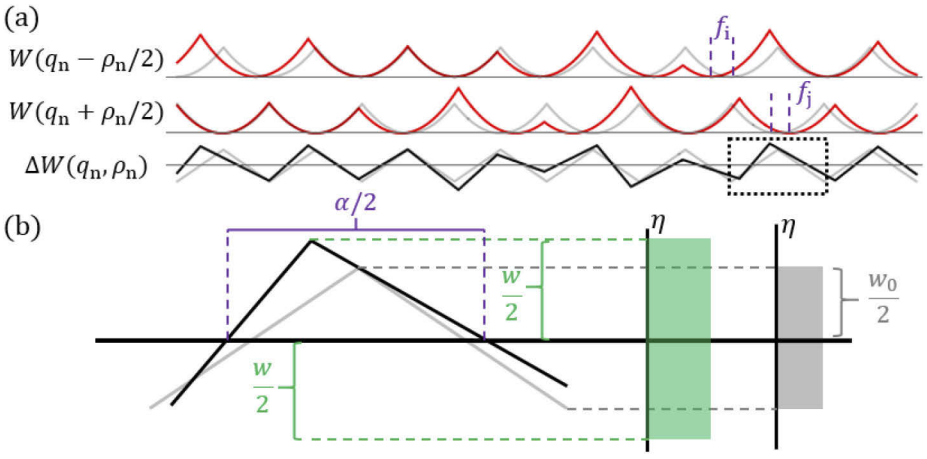

Fig. 5. (a) Two oppositely shifted copies of W, along with their difference ΔW, where f_i and f_j denote the horizontal shift for each parabolic segment of $W(q_n - \rho_n/2)$ and $W(q_n + \rho_n/2)$, respectively. (b) Zoom for one quasi-period, where the effect of feed vibration is to alter both the vertical position of the intersection ($w/2$ instead of the nominal $w_0/2$) and the weight of the contribution to the probability distribution (α/w instead of the nominal T/w_0).

Optics EXPRESS

The lateral displacements of the grooves cause each straight segment of ΔW to provide a different contribution to the PDPD (illustrated by the green rectangle with width w and height α) when compared to the nominal case (gray, with width w_0 and height w_0^{-1}). Due to the statistical symmetry of the intersections, we can make the contributions symmetric around the origin in η to facilitate the calculation. The expressions for w and α are then

$$w(f_i,\, f_{i+1},\, f_j, \rho_\mathrm{n}) = 8h\left(\hat{\rho}_+ + \frac{f_j - f_i}{T}\right)\left(\hat{\rho}_- + \frac{f_{i+1} - f_j}{T}\right), \tag{17}$$

$$\alpha(f_i,\, f_{i+1}) = T + f_{i+1} - f_i, \tag{18}$$

which after averaging lead to the following expression for the PDPD:

$$P_{1,\mathrm{F}}(\eta, \rho_\mathrm{n}) = \frac{1}{T}\iiint_{-\infty}^{\infty} K_\mathrm{F}(f_i)K_\mathrm{F}(f_{i+1})K_\mathrm{F}(f_j)\frac{\alpha(f_i,\, f_{i+1})}{w(f_i,\, f_{i+1},\, f_j)}\mathrm{rect}\left[\frac{\eta}{w(f_i,\, f_{i+1},\, f_j)}\right]\mathrm{d}f_i\mathrm{d}f_{i+1}\mathrm{d}f_j. \tag{19}$$

The Fourier transform of Eq. (19) is given by

$$\tilde{P}_{1,\mathrm{F}}(k, \rho_\mathrm{n}) = \frac{1}{T}\iiint_{-\infty}^{\infty} K_\mathrm{F}(f_i)K_\mathrm{F}(f_{i+1})K_\mathrm{F}(f_j)\,\alpha(f_i,\, f_{i+1})\,\mathrm{sinc}\left[\frac{kw(f_i,\, f_{i+1},\, f_j)}{2}\right]\mathrm{d}f_i\mathrm{d}f_{i+1}\mathrm{d}f_j. \tag{20}$$

Estimated forms of K_F are similar to those reported for K_T [5,9,10]. However, to obtain an analytic result, we assume a zero-mean normal distribution like that in Eq. (15):

$$K_\mathrm{F}(f) = \frac{1}{\sqrt{2\pi}\sigma}\exp\left(-\frac{f^2}{2\sigma^2}\right), \tag{21}$$

Appendix A shows how Eq. (20) can then be solved to give the following expression:

$$\tilde{P}_{1,\mathrm{F}}(k, \rho_\mathrm{n}) = \frac{T\sqrt{\pi}}{8kh\sigma}\mathrm{Re}\left\{\exp\left(-\frac{T^2\hat{\rho}_+^2}{4\sigma^2}\right)\mathrm{erf}[\gamma_+(\rho_\mathrm{n})] + \exp\left(-\frac{T^2\hat{\rho}_-^2}{4\sigma^2}\right)\mathrm{erf}[\gamma_-(\rho_\mathrm{n})]\right\}, \tag{22}$$

where $\mathrm{erf}(u)$ is the error function and

$$\gamma_\pm(\rho_\mathrm{n}) \triangleq \frac{4kh\sigma^2(1 + \hat{\rho}_\mp) + \mathrm{i}T^2\hat{\rho}_\pm}{2\sigma\sqrt{T^2 - 8\mathrm{i}kh\sigma^2 + 48k^2h^2\sigma^4/T^2}}. \tag{23}$$

Figure 6 shows the agreement of $\mathrm{OTF}_\mathrm{perf}(\rho)\mathcal{T}_{\rho_\mathrm{n}}(\tilde{P}_1, \tilde{P}_{1,\mathrm{F}})$ using Eq. (22) with numerically-generated results for several values of σ/T. The estimate is accurate near the local minima, but there is a noticeable discrepancy near the local maxima (where ρ/T is an integer) due to the appearance of an erroneous cusp, clearly visible in the insets of Figs. 6(a)–6(c). This discrepancy arises from the model's assumption about the relative order of the intersections between parabolic segments in the two replicas of W. This assumption is violated for values of ρ_n that fall roughly within σ of each maximum, where the relative order of these intersections can change. [Notice from Fig. 3(d) that a similar behavior, albeit less important, was observed for thrust vibration.] Although a more sophisticated model could be formulated to account for these effects, it would be considerably more complicated, so we propose instead a simple sinusoidal model, based on the observed shape of the numerically-generated OTFs shown in Figs. 6(a)–6(c), namely

$$\tilde{P}_{1,\mathrm{F}}(k, \rho_\mathrm{n}) \approx C_0(\sigma) + C_1(\sigma)\cos\left(\frac{2\pi\rho_\mathrm{n}}{T}\right), \tag{24}$$

where $C_0(\sigma)$ and $C_1(\sigma)$ are chosen so that this sinusoidal coincides with Eq. (22) in regions away from the local maxima. We choose as fitting points the local minima ($\hat{\rho}_+ = \hat{\rho}_- = 1/2$),

Optics EXPRESS

where Eq. (22) is accurate, and points slightly away from the local maxima ($\hat{\rho}_{\pm} = 1/8$). The full expressions are given in Appendix A. It turns out, however, that for $kh < 3/2$ the following simple approximations to those expressions can be used

$$C_0(\sigma) \approx \frac{a_0(kh)}{2} \exp\left(-\frac{3k^2h^2\sigma^2}{T^2}\right) \quad \text{and} \quad C_1(\sigma) \approx a_1(kh) \exp\left(-\frac{22k^2h^2\sigma^2}{T^2}\right), \tag{25}$$

where $a_0(kh)/2$ and $a_1(kh)$, derived in [4], are the coefficients for the Fourier form of $\tilde{P}_1$; note that $C_0(0) = a_0/2$ and $C_1(0) = a_1$. The full expressions of a_0 and a_1 are given in Appendix B. However, for $kh < 3/2$, it is sufficient to use their following truncated Taylor series:

$$a_0(kh) \approx 2 - \frac{8}{45}k^2h^2 \quad \text{and} \quad a_1(kh) \approx \frac{8}{\pi^4}k^2h^2. \tag{26}$$

Figure 6 shows comparisons of the resulting estimate $OTF \approx \mathrm{OTF}_{\mathrm{perf}}(\rho)\mathcal{T}_{\rho_n}(\tilde{P}_1, \tilde{P}_{1,\mathrm{F}})$ with $\tilde{P}_{1,\mathrm{F}}$ given by Eq. (24), with numerical simulations. It is evident that this simple model works well even at the local maxima, where Eq. (22) fails.

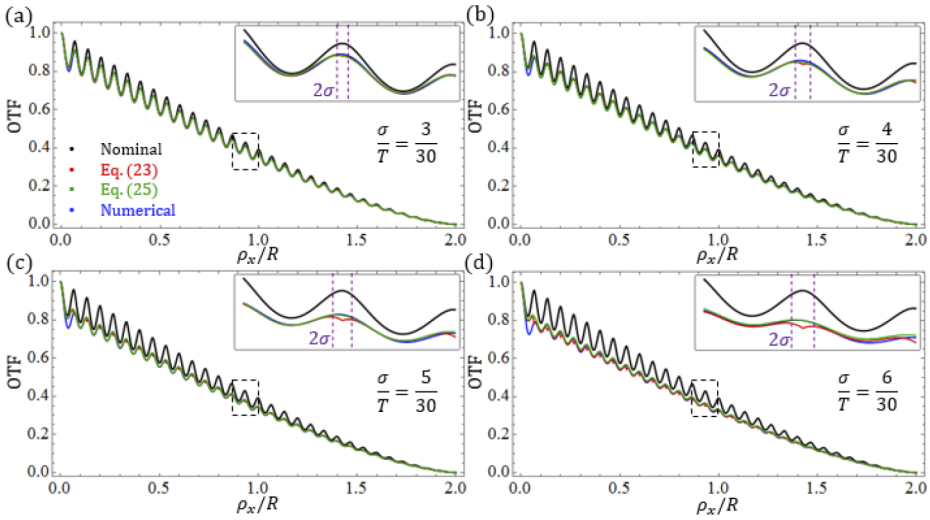

Fig. 6. OTFs for various values of σ/T, for $kh = 1$ and 30 cycles across the aperture. In each part, the nominal OTF (black) corresponds to the case of $\sigma = 0$, the numerical OTF (blue) is generated by averaging the OTFs of 30 randomly generated MSF surfaces [with K_{T} given by Eq. (15)], and the theoretical models (red and green) are calculated from Eqs. (22) and (24), respectively. The insets are zooms of the sections in the dotted black borders, and show the failure of Eq. (22) (red) within a region of width 2σ.

3.4. Combination of thrust and feed vibrations

The combination of the two effects described so far, without the sinusoidal fitting technique discussed in Sec. 3.3, is given by the product of Eqs. (16) and (22):

$$\tilde{P}_{1,\mathrm{C}}(k, \rho_n) = \exp\left[-\frac{k^2\mu^2}{2}\left(\hat{\rho}_+^2 + \hat{\rho}_-^2 + 1\right)\right] \tilde{P}_{1,\mathrm{F}}(k, \rho_n). \tag{27}$$

The effects of thrust vibrations encapsulated in the exponential in Eq. (27) can also be incorporated in the sinusoidal model described after Eq. (23) in order to arrive at a new simple sinusoidal

Optics EXPRESS

model for the combined effects of thrust and feed vibrations:

$$\tilde{P}_{1,\mathrm{C}}(k,\rho_{\mathrm{n}}) \approx G_0(\mu,\sigma) + G_1(\mu,\sigma)\cos\left(\frac{2\pi\rho_{\mathrm{n}}}{T}\right), \tag{28}$$

with $G_0(\mu,\sigma)$ and $G_1(\mu,\sigma)$ given explicitly in Appendix A. For $kh < 3/2$, the expressions for G_0 and G_1 are approximately given by

$$G_0(\mu,\sigma) \approx C_0(\sigma)\exp\left(-\frac{3k^2\mu^2}{4}\right) \quad \text{and} \quad G_1(\mu,\sigma) \approx C_1(\sigma)\exp\left(-k^2\mu^2\right), \tag{29}$$

with $C_0(\sigma)$ and $C_1(\sigma)$ given by their approximations in Eq. (25). The resulting estimate for the OTF, given by $\mathrm{OTF}_{\mathrm{perf}}(\rho)\mathcal{T}_{\rho_{\mathrm{n}}}(\tilde{P}_1,\tilde{P}_{1,\mathrm{C}})$, is compared to numerical simulations in Fig. 7.

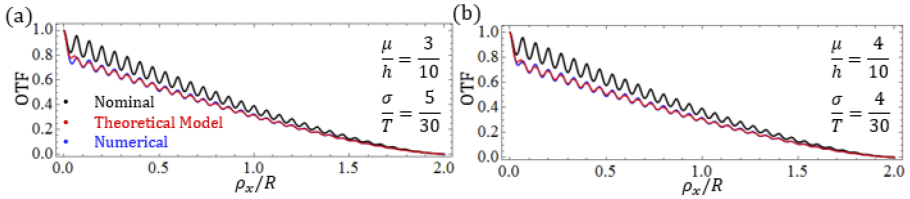

Fig. 7. OTFs for various values of μ/h and σ/T, for $kh = 1$ and 30 cycles across the aperture. In each, the nominal OTF (black) corresponds to the case of $\mu = \sigma = 0$, the numerical OTF (blue) is generated by averaging the OTFs of 75 randomly generated MSF surfaces [with K_{T} given by Eq. (15)], and the theoretical model (red) is calculated from Eq. (27).

3.5. Standard deviation estimate

Tolerancing requires not only an estimate for the mean of the OTF but also for its spread. Based on numerical simulations we propose the following expression for the standard deviation of $\tilde{P}_{1,\mathrm{C}}$ in terms of the dimensionless combinations kh (nominal PV in waves), $2R/T$ (number of cycles), σ/T (relative feed vibration strength), and μ/h (relative thrust vibration strength):

$$\Delta\tilde{P}_{1,\mathrm{C}}(k,\rho_{\mathrm{n}}) \approx \frac{(kh)^2}{2}\left[\frac{30T}{2R}\left(\frac{2\sigma^2}{T^2}+\frac{\mu^2}{2h^2}\right)\right]^{1/2}\tilde{P}_{1,\mathrm{C}}(k,\rho_{\mathrm{n}}). \tag{30}$$

Figure 8 shows the resulting estimate for the standard deviation for the OTF, namely $\pm\Delta\mathrm{OTF}(k,\rho_{\mathrm{n}}) \approx \mathrm{OTF}_{\mathrm{perf}}(\rho)[\mathcal{T}_{\rho_{\mathrm{n}}}(\tilde{P}_1,\tilde{P}_{1,\mathrm{C}}\pm\Delta\tilde{P}_{1,\mathrm{C}}) - \mathcal{T}_{\rho_{\mathrm{n}}}(\tilde{P}_1,\tilde{P}_{1,\mathrm{C}})] = \pm\mathrm{OTF}_{\mathrm{perf}}(\rho)\mathcal{T}_{\rho_{\mathrm{n}}}(0,\Delta\tilde{P}_{1,\mathrm{C}})$, compared with

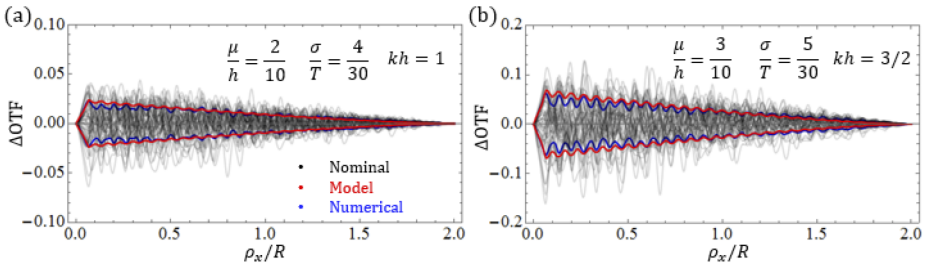

Fig. 8. Estimated (red) and numerically calculated (blue) standard deviation of the OTF for the indicated values of μ/h, σ/T and kh, with 30 cycles across the aperture, based on 50 randomly generated MSF surfaces [with K_{T} given by Eq. (15)]. The difference of the OTF of each realization with the average OTF is shown as a translucent gray curve.

Optics EXPRESS

numerically generated OTF standard deviations assuming normal distributions for K_T and K_F. Of course, OTF_{perf} is an upperbound to OTF + ΔOTF, regardless of Eq. (30).

4. Effects of tool-tip vibrations in MSF structures for turned surfaces

We now extend the model to surfaces with concentric grooves such as those approximating the MSF geometry on diamond-turned surfaces, where the description of the groove shapes given earlier applies to the radial cross section, so that the relevant one-dimensional parameter is $\rho = |\boldsymbol{\rho}|$. As shown in [4], the PDPD for such groove structures can be decomposed in two contributions: one due to the parts of the overlap region where the grooves from two shifted copies of the error align roughly, and one where they do not (as shown in Appendix C.). The latter usually dominates; this gives rise to a strong attenuation of the oscillations in the OTF and makes the effect of variations along the grooves (which break the rotational symmetry) negligible.

4.1. Effects of thrust and feed vibrations

As shown in [4], the (Fourier-transformed) PDPD of a nominal groove structure with turned geometry, $\tilde{P}_2$, can be calculated from the corresponding quantity for the radial cross-section, $\tilde{P}_1$, by expressing the latter as a Fourier series in ρ and multiplying each term by an appropriate factor. Since $\tilde{P}_{1,C}$ in Eq. (28) is already a truncated Fourier series, this transformation is straightforward, and (as shown in Appendix B. with $a_0 \to 2G_0$ and $a_1 \to G_1$) it leads to

$$\tilde{P}_{2,C}(k,\rho) \approx \left\{ G_0(\mu,\sigma) + \frac{G_1(\mu,\sigma)\kappa}{2F(\rho)} \left[A(\rho)\cos\left(\frac{2\pi\rho}{T} - \phi_0\right) + B(\rho)\cos\left(\frac{2\pi\rho}{T} + \phi_0\right) \right] \right\} \times \left\{ [1 - G_0(0,0) - G_1(0,0)C(2)/2]\exp\left(-16\rho^2/T^2\right) + 1 \right\}, \tag{31}$$

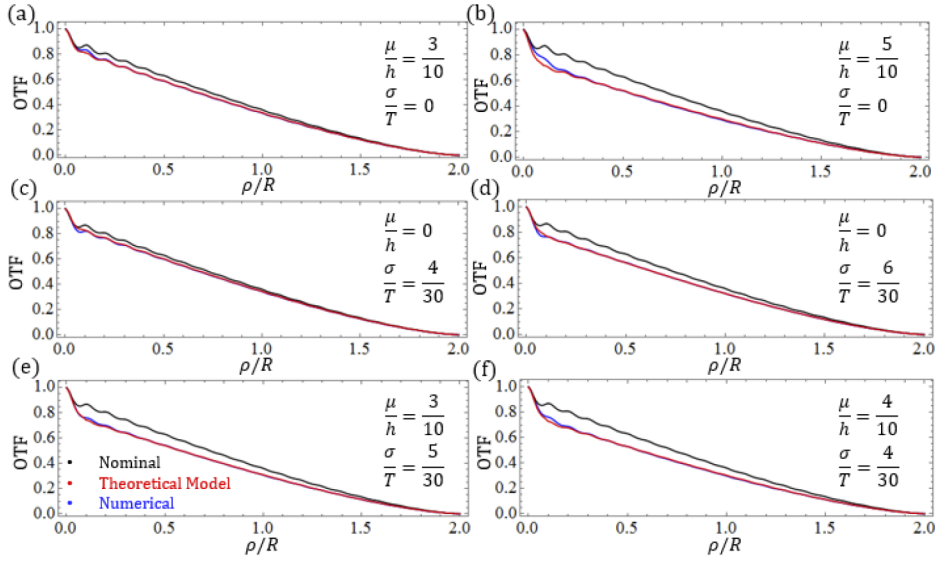

Fig. 9. OTFs for various values of μ/h and σ/T, for $kh = 1$ with 20 cycles across the aperture. In each, the nominal OTF (black) corresponds to the case of $\mu = \sigma = 0$, the numerical OTF (blue) is generated by averaging the OTFs of 75 randomly generated MSF surfaces (with Gaussian statistics), and the theoretical model (red) is calculated from Eq. (31).

Optics EXPRESS

which combines the effects of thrust and feed vibrations in the same manner that Eq. (27) does. Here $\kappa \approx 0.597$ and $\phi_0 \approx \pi/5$ and C is the Fresnel cosine integral. The resulting OTF estimate is given by $\mathrm{OTF}_{\mathrm{perf}}(\rho)\mathcal{T}_\rho(\tilde{P}_2, \tilde{P}_{2,\mathrm{C}})$; this quantity, with $\tilde{K}_\mathrm{T}$ given by Eq. (15), is compared with numerical simulations in Fig. 9. Note that the parts proportional to G_0 and G_1 in Eq. (31) correspond to the average value (baseline) and the oscillations of the OTF, respectively. Since the OTF oscillations for a turned surface are small for low values of kh, it is possible to further approximate $G_1(kh) \approx 0$ in Eq. (31) for an even simpler expression for $\tilde{P}_{2,\mathrm{C}}$.

4.2. Standard deviation estimate

Based on numerical simulations we propose an estimate for the standard deviation of $\tilde{P}_{2,\mathrm{C}}$:

$$\Delta\tilde{P}_{2,\mathrm{C}}(k,\rho) \approx \frac{(kh)^{3/2}}{2\sqrt{3}}\left[\frac{\sqrt{30}}{2R/T}\left(\left\{\frac{8\sigma^2}{T^2}+\frac{\sigma}{T}\right\}^2+\frac{\mu^2}{h^2}\right)\right]^{1/2}\tilde{P}_{2,\mathrm{C}}(k,\rho). \tag{32}$$

Figure 10 shows how $\pm\Delta\mathrm{OTF}(k,\rho) \approx \pm\mathrm{OTF}_{\mathrm{perf}}(\rho)\mathcal{T}_\rho(0,\Delta\tilde{P}_{2,\mathrm{C}})$ compares with numerically generated OTF standard deviations. Once again, $\mathrm{OTF}_{\mathrm{perf}}$ is an upperbound to OTF + ΔOTF.

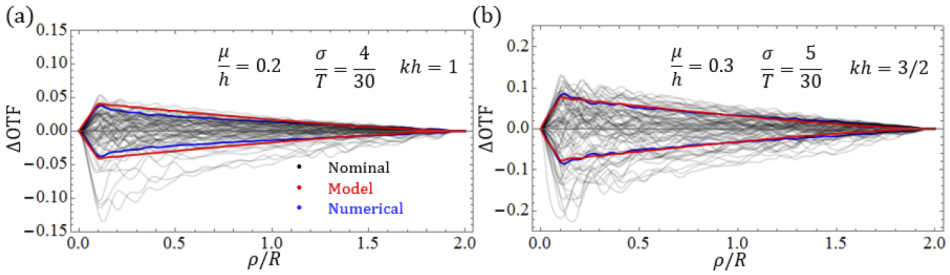

Fig. 10. Estimated (red) and numerically calculated (blue) standard deviation of the OTF for the indicated values of μ/h, σ/T and kh, with 20 cycles across the aperture, based on 50 randomly generated MSF surfaces (with Gaussian statistics). The difference of the OTF of each realization with the average OTF is shown as a translucent gray curve.

5. Summary of results

The OTF estimates derived in this work can be summarized by the following simple expression:

$$\begin{aligned}\mathrm{OTF}(k,\ \boldsymbol{\rho}) \approx \mathrm{OTF}_{\mathrm{perf}}(\rho)\mathfrak{B}(\rho)\Big\{&\mathrm{Max}\left(1-\frac{x}{T},0\right)G_0(0,0)+\mathrm{Min}\left(\frac{x}{T},1\right)G_0(\mu,\sigma)\\&+\left[\mathrm{Max}\left(1-\frac{x}{T},0\right)G_1(0,0)+\mathrm{Min}\left(\frac{x}{T},1\right)G_1(\mu,\sigma)\right]\mathfrak{C}(x)\Big\},\end{aligned} \tag{33}$$

where $x = \boldsymbol{\rho}\cdot\hat{\mathrm{n}}$ for a milled surface with grooves aligned perpendicularly to the unit vector $\hat{\mathrm{n}}$ and $x = \rho = |\boldsymbol{\rho}|$ for a turned surface, $\mathrm{OTF}_{\mathrm{perf}}(\rho)$ is given in Eq. (2), G_0 and G_1 are given by

$$G_0(\mu,\sigma) \approx \left(1-\frac{4}{45}k^2h^2\right)\exp\left(-\frac{3k^2h^2\sigma^2}{T^2}-\frac{3k^2\mu^2}{4}\right), \tag{34}$$

$$G_1(\mu,\sigma) \approx \frac{8}{\pi^4}k^2h^2\exp\left(-\frac{22k^2h^2\sigma^2}{T^2}-k^2\mu^2\right), \tag{35}$$

Optics EXPRESS

$\mathfrak{B}(\rho) \triangleq 1$ and $\mathfrak{B}(\rho) \triangleq 0.07k^2h^2\exp(-16\rho^2/T^2) + 1$ for milled and turned surfaces, respectively, and the oscillatory function $\mathfrak{C}$ is defined as

$$\mathfrak{C}(x) \triangleq \begin{cases} \cos\left(\dfrac{2\pi x}{T}\right) & \text{milled,} \\ \dfrac{0.3}{F(x)}\left[A(x)\cos\left(\dfrac{2\pi x}{T} - \pi/5\right) + B(x)\cos\left(\dfrac{2\pi x}{T} + \pi/5\right)\right] & \text{turned,} \end{cases} \tag{36}$$

where A, B and F are given in Appendix C. Recall that k is the wavenumber, h is the nominal PV of the wavefront error, T is the nominal groove width, and μ and σ are the standard deviations of the the displacements caused by thrust/cutting and feed vibrations, respectively (see Fig. 1).

The corresponding estimates for the standard deviations of the OTFs are given by

$$\Delta\mathrm{OTF}(k,\ x) = \mathrm{OTF}(k,\ x)\,\mathrm{Min}\left(\frac{x}{T}, 1\right)\begin{cases} \dfrac{(kh)^2}{2}\sqrt{\dfrac{30T}{2R}\left(\dfrac{2\sigma^2}{T^2} + \dfrac{\mu^2}{2h^2}\right)} & \text{milled,} \\ \dfrac{(kh)^{3/2}}{2\sqrt{3}}\sqrt{\dfrac{\sqrt{30}T}{2R}\left[\left(\dfrac{8\sigma^2}{T^2} + \dfrac{\sigma}{T}\right)^2 + \dfrac{\mu^2}{h^2}\right]} & \text{turned.} \end{cases} \tag{37}$$

It is important to remember that $\mathrm{OTF}_{\mathrm{perf}}$ is a strict upperbound to OTF + ΔOTF.

6. Concluding remarks

Diamond-machined freeform optical surfaces are inevitably affected by the presence of MSF structures, which cause degradation in optical quality and performance. In this work, we extend the analysis of these errors initiated in [4] by incorporating the effects of vibrations in the thrust, cutting and feed directions, resulting from unwanted relative movement between the diamond tool-tip and the optical element under fabrication. The study was based on a mathematical representation referred to as the PDPD, which allows a geometric/visual interpretation of the effects of these errors.

By working in the PDPD domain, we show how thrust and feed vibrations modify the nominal PDPD through several probability integrals. Although most of the examples presented assumed that the vibrations follow a normal distribution, the theory is general for any probability distribution. Parallel and concentric MSF groove patterns were considered, and expressions for the corresponding mean OTF and spread were given. It should be noted, though, that several approximations were assumed when modeling MSF structures with random variations in both milled and turned geometries. For example, in the consideration of milled surfaces, Eq. (28) does not account for variations along the grooves' direction; these effects can be incorporated by multiplying the result by the Fourier transform of a PDPD describing those variations. Furthermore, for turned surfaces, Eq. (31) does not account for variations that break the rotational symmetry of turned MSF structures; the effect of these variations are negligible.

The results serve to further complement previous tolerancing tools regarding MSF structures found on freeform optical surfaces. Since all realistic diamond-machining processes involve tool-tip vibrations MSF structures, the expressions presented here provide a means to further predict the degradation of the OTF beyond the nominally periodic MSF structures.

Appendix A: Milled feed vibration derivation

We begin by defining the characteristic functions $\tilde{K}_{\mathrm{F}}$ as

$$K_{\mathrm{F}}(f_i) = \frac{1}{2\pi}\int_{-\infty}^{\infty}\tilde{K}_{\mathrm{F}}(p_i)e^{-\mathrm{i}p_i f_i}\,\mathrm{d}p_i. \tag{38}$$

Optics EXPRESS

With this substitution, Eq. (20) becomes a sextuple integral:

$$\tilde{P}_{1,\mathrm{F}}(k,\rho) = \frac{1}{T(2\pi)^3} \iiiint_{-\infty}^{\infty} \tilde{K}_{\mathrm{F}}(p_i)\tilde{K}_{\mathrm{F}}(p_j)\tilde{K}_{\mathrm{F}}(p_{i+1}) e^{-\mathrm{i}(p_i f_i + p_j f_j + p_{i+1} f_{i+1})} \times \alpha(f_i, f_{i+1}) \operatorname{sinc}\left[\frac{kw(f_i, f_j, f_{i+1})}{2}\right] \mathrm{d}f_i \mathrm{d}f_j \mathrm{d}f_{i+1} \mathrm{d}p_i \mathrm{d}p_j \mathrm{d}p_{i+1}. \tag{39}$$

After making a change of variables (with unit Jacobian) from $f_i,\ f_{i+1}$ to $q,\ r$ according to $q = \rho + f_j - f_i,\ r = \rho - T + f_j - f_{i+1}$, the integrals in f_j and p_j can be solved analytically to yield

$$\tilde{P}_{1,\mathrm{F}}(k,\rho) = \frac{1}{T(2\pi)^3} \iint_{-\infty}^{\infty} \tilde{K}_{\mathrm{F}}(p_i)\tilde{K}_{\mathrm{F}}(p_i + p_{i+1})\tilde{K}_{\mathrm{F}}(p_{i+1}) e^{-\mathrm{i}p_i\rho} e^{\mathrm{i}c(T-\rho)} \times \left[\iint_{-\infty}^{\infty} e^{\mathrm{i}p_i q} e^{\mathrm{i}p_{i+1} r} (q-r) \operatorname{sinc}\left(\frac{4kh}{T^2} qr\right) \mathrm{d}q\mathrm{d}r\right] \mathrm{d}p_i \mathrm{d}p_{i+1}. \tag{40}$$

The double integral in the square brackets can also be solved analytically, so that Eq. (40) becomes

$$\tilde{P}_{1,\mathrm{F}}(k,\rho) = -\frac{\mathrm{i}T}{8\pi kh} \iint_{-\infty}^{\infty} \tilde{K}_{\mathrm{F}}(p_i)\tilde{K}_{\mathrm{F}}(p_i + p_{i+1})\tilde{K}_{\mathrm{F}}(p_{i+1}) e^{-\mathrm{i}p_i\rho} e^{\mathrm{i}c(T-\rho)} \times \cos\left(\frac{p_i p_{i+1} T^2}{4kh}\right)\left(\frac{1}{p_i} - \frac{1}{p_{i+1}}\right) \mathrm{d}p_i \mathrm{d}p_{i+1}. \tag{41}$$

By assuming the Gaussian form for K_{F} in Eq. (15), Eq. (41) can be solved to give Eq. (22).

The exact forms of the coefficients C_0 and C_1 in Eq. (24) are given by

$$C_0(\sigma) = \frac{T\sqrt{\pi}}{(1+\sqrt{2})8kh\sigma}\left(\sqrt{2}\mathrm{Re}\left\{\exp\left(-\frac{T^2}{256\sigma^2}\right)\operatorname{erf}\left[\gamma_+\left(\frac{T}{8}\right)\right] + \exp\left(-\frac{49T^2}{256\sigma^2}\right)\operatorname{erf}\left[\gamma_-\left(\frac{T}{8}\right)\right]\right\} + 2\exp\left(-\frac{T^2}{16\sigma^2}\right)\mathrm{Re}\left[\operatorname{erf}(\gamma_0)\right]\right), \tag{42}$$

$$C_1(\sigma) = \frac{(2-\sqrt{2})T\sqrt{\pi}}{8kh\sigma}\left(\mathrm{Re}\left\{\exp\left(-\frac{T^2}{256\sigma^2}\right)\operatorname{erf}\left[\gamma_+\left(\frac{T}{8}\right)\right] + \exp\left(-\frac{49T^2}{256\sigma^2}\right)\operatorname{erf}\left[\gamma_-\left(\frac{T}{8}\right)\right]\right\} - 2\exp\left(-\frac{T^2}{16\sigma^2}\right)\mathrm{Re}\left[\operatorname{erf}(\gamma_0)\right]\right), \tag{43}$$

for $\gamma_0 \triangleq \gamma_+(T/2) = \gamma_-(T/2)$. The corresponding forms for G_0 and G_1 in Eq. (28) are

$$G_0(\mu,\sigma) = \frac{T\sqrt{\pi}}{(1+\sqrt{2})8kh\sigma}\left(\sqrt{2}\mathrm{Re}\left\{\exp\left(-\frac{T^2}{256\sigma^2}\right)\operatorname{erf}\left[\gamma_+\left(\frac{T}{8}\right)\right] + \exp\left(-\frac{49T^2}{256\sigma^2}\right)\operatorname{erf}\left[\gamma_-\left(\frac{T}{8}\right)\right]\right\} + 2\exp\left(\frac{9k^2\mu^2}{64}\right)\exp\left(-\frac{T^2}{16\sigma^2}\right)\mathrm{Re}\left[\operatorname{erf}(\gamma_0)\right]\right)\exp\left(-\frac{57k^2\mu^2}{64}\right), \tag{44}$$

$$G_1(\mu,\sigma) = \frac{(2-\sqrt{2})T\sqrt{\pi}}{8kh\sigma}\left(\mathrm{Re}\left\{\exp\left(-\frac{T^2}{256\sigma^2}\right)\operatorname{erf}\left[\gamma_+\left(\frac{T}{8}\right)\right] + \exp\left(-\frac{49T^2}{256\sigma^2}\right)\operatorname{erf}\left[\gamma_-\left(\frac{T}{8}\right)\right]\right\} - 2\exp\left(\frac{9k^2\mu^2}{64}\right)\exp\left(-\frac{T^2}{16\sigma^2}\right)\mathrm{Re}\left[\operatorname{erf}(\gamma_0)\right]\right)\exp\left(-\frac{57k^2\mu^2}{64}\right). \tag{45}$$

Optics EXPRESS

Appendix B: Review of PDPD theory for diamond-turned surfaces

This appendix summarizes the results in [4] for finding the Fourier transform of the PDPD for turned surfaces ($\tilde{P}_2$) from that for milled surfaces ($\tilde{P}_1$) with the same cross-section, and provides corrections to two typographic errors in [4]. This relation was found to take the form

$$\tilde{P}_2(k,\rho) = \frac{1}{F(\rho)}\left[\frac{A(\rho)}{2}\hat{Q}_t\tilde{P}_1(k,\rho) + \frac{B(\rho)}{2}\hat{Q}_\tau\tilde{P}_1(k,\rho) + E(\rho)\tilde{P}_0(k)\right], \tag{46}$$

where A, B, E and F represent specific areas within the overlap of the two shifted circular aperture copies whose expressions are given in Appendix C., the integral operator $\hat{Q}_x$ is defined as

$$\hat{Q}_x f(\rho) = \int_0^1 \frac{f(\rho - xv)}{\sqrt{v}}\,\mathrm{d}v, \tag{47}$$

for x given by either $t = \mathrm{Min}(\rho, T)$ or $\tau = -\mathrm{Min}(2R - \rho, T)$, and $\tilde{P}_0(k) \triangleq \int_0^T \tilde{P}_1(k,\rho)\,\mathrm{d}\rho/T$ is the average value of $\tilde{P}_1$ over one period. Please note that the equations in [4] corresponding to Eq. (46) included an erroneous extra factor of $\sqrt{2}$ in the prefactor of $B(\rho)$, and the expressions in [4] for the areas A, B and E included some errors that are now corrected in Appendix C.

The action of $\hat{Q}_x$ is simplest to calculate if $\tilde{P}_1$ is expressed as a Fourier series:

$$\tilde{P}_1(k,\rho) = \frac{a_0}{2} + \sum_{m=1}^{\infty} a_m \cos\left(\frac{2\pi m\rho}{T}\right), \tag{48}$$

The Fourier series following the transformation is given by

$$\begin{aligned}\hat{Q}_x\tilde{P}_1(k,\rho) &= a_0 \\ &+ \sqrt{\frac{T}{|x|}}\sum_{m=1}^{\infty}\frac{a_m}{\sqrt{m}}\left[C\left(2\sqrt{\frac{m|x|}{T}}\right)\cos\left(\frac{2\pi m\rho}{T}\right) + \mathrm{sgn}(x)S\left(2\sqrt{\frac{m|x|}{T}}\right)\sin\left(\frac{2\pi m\rho}{T}\right)\right],\end{aligned} \tag{49}$$

where C and S are the Fresnel cosine and sine integrals. For MSF with moderate PV errors, the first two terms in the series in Eq. (49) are dominant, so we can use the approximation

$$\tilde{P}_2(k,\rho) \approx \frac{a_0}{2} + a_1\left[\mathcal{P}_\mathrm{C}(\rho)\cos\left(\frac{2\pi\rho}{T}\right) + \mathcal{P}_\mathrm{S}(\rho)\sin\left(\frac{2\pi\rho}{T}\right)\right], \tag{50}$$

where

$$\mathcal{P}_\mathrm{C}(\rho) \triangleq \frac{1}{2F(\rho)}\left[A(\rho)\sqrt{\frac{T}{t}}C\left(2\sqrt{\frac{t}{T}}\right) + B(\rho)\sqrt{\frac{T}{\tau}}C\left(2\sqrt{\frac{\tau}{T}}\right)\right], \tag{51}$$

$$\mathcal{P}_\mathrm{S}(\rho) \triangleq \frac{1}{2F(\rho)}\left[A(\rho)\sqrt{\frac{T}{t}}S\left(2\sqrt{\frac{t}{T}}\right) - B(\rho)\sqrt{\frac{T}{\tau}}S\left(2\sqrt{\frac{\tau}{T}}\right)\right]. \tag{52}$$

Aside from the first and last periods [$\rho \in (0,T) \cup (2R-T, 2R)$], t/T and τ/T are unity. Since we consider the first period separately later, and the OTF of the last period is strongly attenuated by the prefactor OTF_{perf}, we can simply use $t/T = \tau/T = 1$ leading to the approximations

$$\mathcal{P}_\mathrm{C}(\rho) \approx \frac{A(\rho)C(2) + B(\rho)C(2)}{2F(\rho)} \quad \text{and} \quad \mathcal{P}_\mathrm{S}(\rho) \approx \frac{A(\rho)S(2) - B(\rho)S(2)}{2F(\rho)}. \tag{53}$$

Using Eqs. (53) and simple trigonometric identities, Eq. (50) can be written as

$$\tilde{P}_2(k,\rho) \approx \frac{a_0}{2} + \frac{a_1\kappa}{2F(\rho)}\left[A(\rho)\cos\left(\frac{2\pi\rho}{T} - \phi_0\right) + B(\rho)\cos\left(\frac{2\pi\rho}{T} + \phi_0\right)\right], \tag{54}$$

where $\kappa = \sqrt{C^2(2) + S^2(2)} \approx 0.597$ and $\phi_0 = \tan^{-1}[S(2)/C(2)] \approx \pi/5$. To ensure that the value of the OTF is unity at $\rho = 0$, the erroneous assumption that $t/T = \tau/T = 1$ for the first period can be patched up with a factor of $[1 - a_0/2 - a_1C(2)/2]\exp\left(-16\rho^2/T^2\right) + 1$, as seen in Eq. (31).

Optics EXPRESS

Note that, for $\mu = 0$ and $\sigma = 0$, a_m were found in [4] to be given by

$$a_m = \frac{\pi}{8kh}\left|\text{erfi}\left[\frac{(1+\text{i})(2kh - m\pi)}{4\sqrt{kh/2}}\right] + \text{erfi}\left[\frac{(1+\text{i})(2kh + m\pi)}{4\sqrt{kh/2}}\right]\right|^2, \tag{55}$$

where erfi(u) is the imaginary error function. Equations (26) give the truncated (to second order) Taylor series of $a_0(kh)$ and $a_1(kh)$, which are a valid approximation for $kh \lesssim 3/2$.

Appendix C: Definitions of overlap area functions

The area functions $A(\rho)$ and $B(\rho)$ are given for $\rho < R$ by

$$A(\rho) = \frac{1}{8}\left\{4R^2\cos^{-1}\left[\frac{\rho\left(V^2 + X_+\right)}{2RU_+^2}\right] - \rho V\cosh^{-1}\left(\frac{X'_+}{U_+^2}\right) - \frac{\rho V}{U_+^2}\sqrt{X_{+'}^2 - U_+^4}\right\} \tag{56}$$

$$B(\rho) = \pi\rho V/16, \tag{57}$$

while for $\rho \geq R$ they are

$$A(\rho) = 0 \tag{58}$$

$$B(\rho) = \frac{1}{8}\left\{2\pi R^2 - 4R^2\sin^{-1}\left(\frac{2R\rho}{V^2 + X_-}\right) - \rho V\sin^{-1}\left(\frac{X'_-}{U_-^2}\right) + \frac{\rho V}{U_-^2}\sqrt{U_-^4 - X_{-'}^2}\right\}, \tag{59}$$

where

$$V = \sqrt{T(T+2\rho)}, \quad U_\pm = \sqrt{V^2 \pm \rho^2}, \quad X_\pm = \sqrt{V^4 \pm 4R^2U_\pm^2}, \quad X'_\pm = X_\pm - \rho^2. \tag{60}$$

For all $\rho \in [0, 2R]$, we have

$$F(\rho) = \frac{1}{2}\left[R^2\arccos\left(\frac{\rho}{2R}\right) - \frac{\rho}{2}\sqrt{R^2 - \left(\frac{\rho}{2}\right)^2}\right] = \frac{\pi R^2}{4}\text{OTF}_{\text{perf}}(\rho). \tag{61}$$

Figure 11 shows a graphical representation of $A(\rho), B(\rho)$, and $E(\rho) = F(\rho) - A(\rho) - B(\rho)$ as the areas of the blue, red, and green regions, respectively.

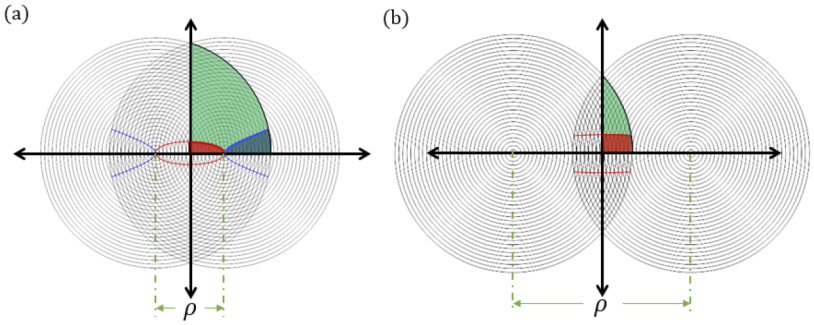

Fig. 11. The overlap area between two shifted copies of a circular pupil is divided into A, B, and E (blue, red, and green). (a) and (b) show the cases of $\rho \leq R$ and $\rho > R$, respectively.

Funding

National Science Foundation (NSF) I/UCRC Center for Freeform Optics (IIP-1338877); Aix-Marseille Université.

Optics EXPRESS

Acknowledgments

MAA received funding from the Excellence Initiative of Aix-Marseille University – A*MIDEX, a French "Investissements d'Avenir" programme.

Disclosures

The authors declare that there are no conflicts of interest related to this article.

References

1. J. M. Tamkin, T. D. Milster, and W. Dallas, "Theory of modulation transfer function artifacts due to mid-spatial-frequency errors and its application to optical tolerancing," Appl. Opt. **49**(25), 4825–4835 (2010).
2. G. W. Forbes, "Never-ending struggles with mid-spatial frequencies," Proc. SPIE **9525**, 95251B (2015).
3. K. Liang and M. A. Alonso, "Effects of defocus and other quadratic errors on OTF," Opt. Lett. **42**(24), 5254–5257 (2017).
4. K. Liang and M. A. Alonso, "Understanding the effects of groove structures on the OTF," Opt. Express **25**(16), 18827–18841 (2017).
5. H. Wang, S. To, C. Y. Chan, C. F. Cheung, and W. B. Lee, "A theoretical and experimental investigation of the tool-tip vibration and its influence upon surface generation in single-point diamond turning," Int. J. Mach. Tools Manufact. **50**(3), 241–252 (2010).
6. H. Wang, S. To, and C. Y. Chan, "Investigation on the influence of tool-tip vibration on surface roughness and its representative measurement in ultra-precision diamond turning," Int. J. Mach. Tools Manufact. **69**, 20–29 (2013).
7. S. J. Zhang and S. To, "A theoretical and experimental study of surface generation under spindle vibration in ultra-precision raster milling," Int. J. Mach. Tools Manufact. **75**, 36–45 (2013).
8. S. Takasu, M. Masuda, and T. Nishiguchi, "Influence of Study Vibration with Small Amplitude Upon Surface Roughness in Diamond Machining," CIRP Ann. **34**(1), 463–467 (1985).
9. D. L. Martin, A. N. Tabenkin, and F. G. Parsons, "Precision Spindle and Bearing Error Analysis," Int. J. Mach. Tools Manufact. **35**(2), 187–193 (1995).
10. D. Kim, I. Chang, and S. Kim, "Microscopic topographical analysis of tool vibration effects on diamond turned optical surfaces," Precis. Eng. **26**(2), 168–174 (2002).
11. J. W. Goodman, *Introduction to Fourier Optics* (Roberts & Company, 2005), Chap. 6.